CFD Modelling of Microclimates in Photovoltaic Integrated Green Roofs

Haoran Chang [a], Mengying Li [b] and Zhaojian Liang [c]

[a] Department of Mechanical Engineering & Research Institute for Smart Energy, The Hong Kong Polytechnic University, Hong Kong SAR, haoran1.chang@connect.polyu.hk
[b] Department of Mechanical Engineering & Research Institute for Smart Energy, The Hong Kong Polytechnic University, Hong Kong SAR, mengying.li@polyu.edu.hk
[c] School of Energy and Environment, City University of Hong Kong, Hong Kong SAR, zhaojian.liang@cityu.edu.hk

Abstract:

Photovoltaic-integrated green roofs (PVIGR) combine rooftop solar power generation with ecological and thermal benefits, but the coupled interactions among PV modules, vegetation, and surrounding environment remain poorly understood. This study develops a three-dimensional transient multi-physics CFD model for a full-scale PVIGR with three PV rows above a vegetated roof, incorporating turbulent airflow, heat and moisture transfer, plant transpiration, and radiative exchange. A conventional rooftop photovoltaic (RPV) system without vegetation is used as a reference. Simulations for summer rooftop conditions in Hong Kong from 10:00 to 12:00 on August 3, 2024 show that vegetation increases aerodynamic resistance and weakens airflow beneath the PV modules, especially in downstream rows. As a result, PVIGR modules in most downstream locations operate at higher temperatures than those in the RPV case, with a peak temperature of about 340 K, roughly 5 K higher after two hours. Meanwhile, the vegetated roof remains cooler than the concrete roof due to transpiration, with surface temperatures averaging 3 K lower and up to 7 K lower in well-ventilated windward areas. Humidity within the PVIGR is highly heterogeneous, remaining near saturation inside the canopy but having limited influence on the broader rooftop air. PV shading also strongly redistributes solar radiation, reducing irradiance in shaded vegetation to about 12% of unshaded levels and substantially suppressing latent heat flux and water loss. These results show that PVIGR performance depends on tightly coupled airflow, radiation, heat transfer, and plant transpiration, and that vegetation does not necessarily improve PV thermal performance without sufficient sub-module ventilation. The model provides a high-fidelity tool for optimizing PVIGR design for both energy and environmental performance.

Keywords:

The photovoltaic integrated green roof; 3D numerical model; Microenvironment.

1. Introduction

Rapid urbanization has significantly intensified the Urban Heat Island (UHI) effect [1], primarily due to the replacement of natural landscapes with heat-absorbing building materials and the resulting depletion of urban greenery. To address escalating energy demands and transition toward carbon neutrality, rooftop photovoltaic (RPV) systems [2] have emerged as a critical solution for distributed renewable power generation. However, PV modules often incur a substantial thermal penalty: due to their high solar absorptance and relatively low conversion efficiency, they can act as secondary heat sources, raising local temperatures by more than 20°C [3]. Photovoltaic-integrated green roofs (PVIGR) offer a promising synergistic alternative [4] by vertically coupling PV modules with vegetated layers. In these integrated systems, plant transpiration provides an effective cooling mechanism that lowers module operating temperatures and enhances electrical efficiency [5], while the PV panels provide protective shading that shields vegetation from excessive solar radiation and reduces evaporative water loss [6].

Understanding the internal microclimate of PVIGR systems is of paramount importance, as the vertical coupling of plant biological functions and PV thermal behavior creates a localized environment that directly governs both electrical efficiency and ecological health. While field experiments provide essential real-world data, numerical simulation is indispensable for resolving the intricate, interdependent physical drivers within these systems and for performing the parametric optimizations required for practical implementation. Currently, the research landscape is predominantly defined by experimental studies. For instance, [7] conducted field evaluations in Mediterranean climates, and [8] demonstrated a 2% increase in electricity production efficiency

in tropical environments. Early foundational work by [9] similarly reported that green roofs could enhance PV electricity generation by approximately 6% compared to conventional roofs. Existing numerical investigations have primarily focused on city-scale energy benefits or the quantification of overall power generation gains. For example, [10] utilized EnergyPlus to compare annual building energy consumption, while [11] and [12] developed models to predict annual PV yields and shading impacts. However, these studies typically treat the system as a collection of standalone units or simplify the physical interactions to prioritize macro-scale performance metrics.

Despite the recognized synergistic benefits of PVIGR systems, a critical research gap persists regarding the high-fidelity characterization of the collective microclimate within extensive multi-row arrays. Resolving the interdependent physical drivers at this scale, including turbulent airflow through porous vegetation, transpiration-driven moisture transport, and non-uniform radiative exchange, presents significant modelling challenges. To address this gap, this study develops a holistic three-dimensional (3D) transient multi-physics Computational Fluid Dynamics (CFD) model to simulate the microenvironment of a PVIGR system comprising a three-row PV array. This framework provides insight into the mechanisms underlying PV-vegetation interactions under realistic installation conditions.

2. Methodology

The microenvironment within PVIGR systems is governed by a complex interplay of multi-physics interactions, where localized thermal and aerodynamic behaviors emerge from the synergy between PV modules and the underlying vegetation. To resolve these intricate dynamics, a holistic 3D transient numerical model is developed using a CFD framework. This modelling approach simultaneously accounts for turbulent airflow in free and porous media, non-uniform radiative exchange (including solar shading and longwave thermal radiation), and moisture transport driven by plant transpiration and soil evaporation. The conceptual modeling framework is schematically shown in Fig. 1, which depicts the constituent physical fields and the associated heat and mass transfer processes within the integrated system.

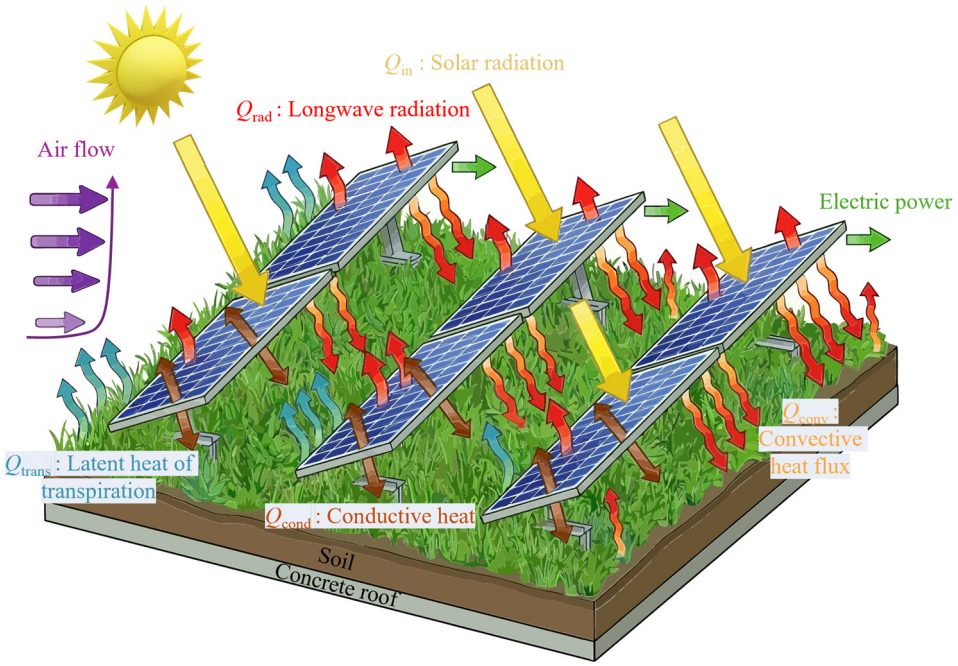

Figure. 1. *Schematic diagram of the PVIGR system and related physical processes.*

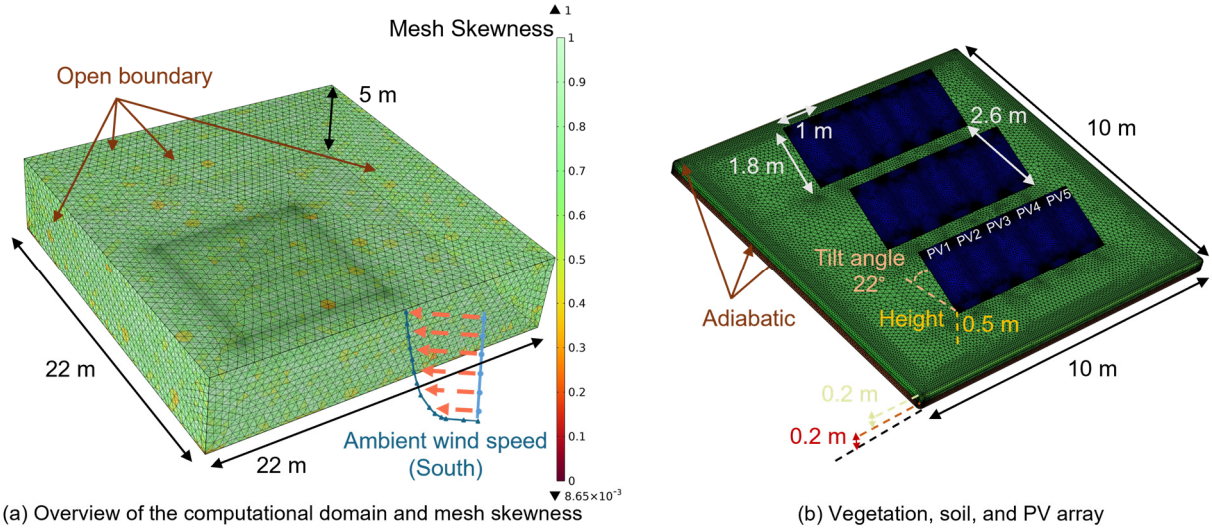

(a) Overview of the computational domain and mesh skewness

(b) Vegetation, soil, and PV array

Figure. 2. *Geometry of the modelling domain, mesh scheme, and dimensions.*

This study utilizes COMSOL Multiphysics to simulate the microclimate of the PVIGR system, enabling high-fidelity characterization of the PV-vegetation synergy at a full-scale array level. The computational geometry and mesh discretization adopted in this study are shown in Fig. 2. The PVIGR system is centred within a computational domain of 22 m × 22 m × 5 m to provide sufficient space for airflow development and to minimize boundary effects. Within this domain, the rooftop PV array is configured to represent a typical installation, consisting of three rows with five modules in each row. Each module has dimensions of 1.85 m × 1.03 m × 0.003 m, is mounted at a fixed tilt angle of 22° and is elevated 0.5 m above the vegetation layer. A row spacing of 2.6 m is prescribed to avoid inter-row shading and maintain uniform solar exposure. The PV array is positioned directly above a porous vegetated region measuring 10 m × 10 m × 0.4 m, which represents the green roof canopy alongside its underlying soil substrate. In the numerical model, the air domain, vegetation, soil, and PV modules are geometrically simplified as cuboidal regions, while the PV modules retain a multilayer structure consistent with the material properties and specifications of the actual devices. A refined mesh is employed in the vicinity of the integrated system to ensure numerical stability and solution accuracy.

2.1. Free and porous media flow

The airflow in the computational domain is described using the Reynolds averaged Navier Stokes equations, which provide a computationally efficient means of capturing mean flow characteristics. The shear stress transport (SST) *k*−*ω* model is selected to solve the turbulent flow field because of its high accuracy in near wall regions and stability in free flow domains. Within this framework, the turbulent flow field is solved using turbulent kinetic energy (as shown in Eq. (1)) and specific dissipation rate (as shown in Eq. (2)) as the primary variables.

$$\rho\frac{\partial k}{\partial t}+\rho\mathrm{u}\cdot\nabla k=P-\rho\beta_0^*k\omega+\nabla\cdot((\mu+\sigma_k\mu_\mathrm{T})\nabla k) \qquad (1)$$

$$\rho\frac{\partial \omega}{\partial t}+\rho\mathrm{u}\cdot\nabla \omega=\frac{\rho\gamma}{\mu_\mathrm{T}}P-\rho\beta_1^*\omega^2+\nabla\cdot((\mu+\sigma_{\omega1}\mu_\mathrm{T})\nabla\omega)+2(1-f_v)\frac{\rho\sigma_{\omega2}}{\omega}\nabla\omega\cdot\nabla k \qquad (2)$$

Airflow within the vegetated region is modelled as flow through a porous medium using the Brinkman equation. A Forchheimer resistance term is included to represent the drag imposed by leaves as a velocity-squared body force. The porous properties of the vegetation, including porosity and permeability, are derived from the leaf area index. Air is assumed to be an incompressible Newtonian fluid, and buoyancy effects in the non-isothermal flow are incorporated using the Boussinesq approximation.

$$\frac{\partial}{\partial t}(\varepsilon_\mathrm{p}\rho)+\nabla\cdot(\rho\mathrm{u})=Q_\mathrm{m} \qquad (3)$$

$$\frac{\rho}{\varepsilon_{\mathrm{p}}}\left(\frac{\partial \mathrm{u}}{\partial t}+(\mathrm{u}\cdot\nabla)\frac{\mathrm{u}}{\varepsilon_{\mathrm{p}}}\right)=-\nabla p+\nabla\cdot\left[\frac{1}{\varepsilon_{\mathrm{p}}}\left\{\mu(\nabla\mathrm{u}+(\nabla\mathrm{u})^{\mathrm{T}})-\frac{2}{3}\mu(\nabla\cdot\mathrm{u})\mathrm{I}\right\}\right]-\left(\kappa^{-1}\mu+\frac{Q_{\mathrm{m}}}{\varepsilon_{\mathrm{p}}{}^{2}}\right)\mathrm{u}+\mathrm{F} \quad (4)$$

2.2. Moisture transport in moist air and porous medium

Moisture transport in the PVIGR system involves the evolution of water vapor concentration in the air and the vapor transport within the porous vegetation layer. Spatiotemporal variations in vapor concentration are assumed small enough that they do not significantly affect the density of moist air. Under the dilute species assumption, the mass conservation equation for water vapor in air accounts for convection, binary diffusion, and a volumetric moisture source G. The governing equation for the air domain is defined as:

$$M_v\frac{\partial c_v}{\partial t}+M_v\mathrm{u}\cdot\nabla c_v+\nabla\cdot g_w=G \quad (5)$$

In the porous vegetation domain, moisture exists in both vapor and liquid phases. The mass conservation equations for liquid water and water vapor are combined into a single equation to describe the overall moisture transport under two-phase coexistence. This process is formulated as:

$$\frac{\partial w(\phi)}{\partial t}+\nabla\cdot(\omega_{\mathrm{v}}\rho_{\mathrm{g}}\mathrm{u}_{\mathrm{g}})+\nabla\cdot g_{\mathrm{w}}+\nabla\cdot(\rho_{\mathrm{l}}\mathrm{u}_{\mathrm{l}})+\nabla\cdot g_{\mathrm{lc}}=G \quad (6)$$

The volumetric source term for the vegetation domain is defined by the mass of water vapor produced per unit plant volume per second. Because transpiration occurs throughout the canopy rather than solely on the surface, this term is calculated as the product of the vapor generation rate and the leaf area density (LAD).

$$G=E_c\cdot LAD=\frac{c_{leaf}-c_v}{r_{\mathrm{s}}+r_{\mathrm{a}}}\cdot LAD \quad (7)$$

The boundary layer resistance r_a is determined using empirical equations for a horizontal flat plate based on the wind speed u. When u is lower than 0.1 m/s, r_a is calculated from the temperature difference between the leaf and the environment as $r_a = 840(d/|T-T\infty|)^{0.25}$, while for higher wind speeds it is defined as $r_a = 220d^{0.2}/ u_a^{0.8}$ [13], where d is the characteristic length of the leaf. The stomatal resistance r_s is modeled as a function of shortwave solar radiation and vapor pressure deficit to reflect the physiological response of the vegetation to sunlight and humidity. This resistance is calculated using a semi-empirical relationship [14] as follows:

$$r_{\mathrm{s}}=r_{\mathrm{s,min}}\cdot\frac{a_1+Q_{r,s-w}}{a_2+Q_{r,s-w}}\cdot[1+a_3(D-D_0)^2] \quad (8)$$

2.3. Heat transfer in moist air and porous medium

Heat transfer within the system is modeled by solving the energy conservation equations for both the air and porous vegetation domains. In the moist air domain, the model accounts for conduction, convection, and radiative exchange while incorporating an additional term to represent the diffusive flux of thermal enthalpy arising from concentration gradients. The governing equation for the air domain is defined as:

$$\rho C_p\left(\frac{\partial T}{\partial t}+\mathrm{u}\cdot\nabla T\right)+\nabla\cdot(q+q_r)=\left(\frac{\partial p}{\partial t}+\mathrm{u}\cdot\nabla p\right)+\tau:\nabla\mathrm{u}+Q_{\mathrm{H}}+Q_{\mathrm{V}}+Q_{\mathrm{PV}} \quad (9)$$

For the porous vegetation domain, the model assumes local thermal equilibrium between the solid plant matrix, moist air, and liquid water. The heat transfer process in this multiphase medium is described by a single energy equation utilizing effective thermophysical properties to account for the combined contributions of component diffusion, capillary flow, and phase change.

$$(\rho C_p)_{\text{eff}} \frac{\partial T}{\partial t} + (\rho_g C_{p,g} \mathrm{u}_g + \rho_\mathrm{l} C_{p,\mathrm{l}} \mathrm{u}_\mathrm{l}) \cdot \nabla T + \nabla \cdot q = Q_\mathrm{S} + Q_\mathrm{H} + Q_\mathrm{V} \qquad (10)$$

In this formulation, Q_S represents the latent-heat sink associated with soil-moisture evaporation at the substrate surface. Q_V quantifies the latent heat removed through plant transpiration, while Q_H accounts for the enthalpy diffusive flux and liquid capillary flux within the canopy.

The thermal effect of the PV modules is represented by volumetric heat sources (Q_PV) in the glass, EVA, and solar cell layers. This treatment accounts for radiation attenuation through the module structure by assigning energy absorption according to the solar absorptance of each layer. For the solar cell, the absorbed fraction converted into electricity is excluded from the heat source term. Each module is assumed to have a rated power of 400 W and a reference conversion efficiency of 21.25% under standard test conditions, with efficiency decreasing as operating temperature increases.

2.4. Solar and surface-to-surface radiation

The radiation module simulates the transfer of solar radiation within the system, incorporating the shading effects of the PV array and the longwave radiative exchange among component surfaces. Radiative properties are classified into shortwave and longwave bands using a 2.5 micrometre wavelength threshold. Surfaces are treated as diffuse grey surfaces where the radiosity is determined through an equilibrium formulation:

$$J_i = \rho_{d,i}(G_{m,i} + G_{ext,i} + G_{amb,i}) + \varepsilon_{s,i}\sigma T_i^4 \qquad (11)$$

In this equation, J_i is the radiosity and $\rho_{d,i}$ is the diffuse reflectance. The term $G_{m,i}$ represents the mutual radiation exchange between the PV modules and the underlying vegetation, with view factors calculated using the hemicube method. Ambient environmental radiation is represented by $G_{amb,i}$. To capture the realistic solar irradiation distribution under the shading of the multi-row array, the external irradiation $G_{ext,i}$ is decomposed into direct and diffuse components:

$$G_{ext,i} = q_{s,i} + I_{diff} \qquad (12)$$

where $q_{s,I}$ is the incident direct solar radiation and I_{diff} is the diffuse atmospheric radiation. During transient simulations, the model calculates the irradiance received by the vegetation at each time step, accounting for the changing position of the sun relative to the PV modules. This approach enables the model to capture dynamic shading and the resulting non-uniform radiation field beneath the array. These radiative fluxes are coupled with heat and moisture transport, since solar input directly influences plant temperature and transpiration. The inclusion of diffuse radiation further improves the representation of irradiance received by shaded vegetation.

3. Results and discussion

Based on the developed multi-physics framework, this section evaluates the microclimatic performance of the proposed PVIGR system under representative environmental conditions. To isolate the effect of vegetation, a reference RPV case is constructed by removing the soil and plant layers while keeping all other boundary conditions unchanged. Local thermal equilibrium is assumed within the porous vegetation domain. To reduce computational cost, the module mounting pillars are neglected because their aerodynamic influence is minor relative to that of the modules and vegetation. The vegetation layer is represented by Sedum lineare, with a fixed LAD [15] of 23 and porosity of 0.6, which determine the aerodynamic resistance and transpiration characteristics of the canopy.

Boundary conditions are prescribed to represent a realistic urban rooftop environment. The inlet wind is defined by a power-law profile to capture the near-roof velocity gradient, while the lateral and top boundaries are treated as open to allow mass and heat exchange with the surroundings. To resolve the temporal evolution of the microclimate, a two-hour transient simulation from 10:00 a.m. to 12:00 p.m. is performed, with environmental variables updated hourly. Meteorological inputs are based on typical summer conditions derived from Hong Kong Observatory data for August 3, 2024. The model also incorporates the changing solar position during the simulation period, and the corresponding environmental inputs are summarized in Table 1.

Table 1. *Input variables for the two-hour transient simulation.*

Variable	Unit	Hour 1	Hour 2

Ambient temperature	K	304.01	304.42
Sky temperature	K	298.92	299.72
Relative humidity	%	71.83	72.43
Inlet wind speed (at 2m)	m/s	1	1
Wind direction	°	180	180
Direct solar radiation	W/m^2	789.85	849.55
Diffuse solar radiation	W/m^2	108.40	103.53
Plane of Array irradiance	W/m^2	710.02	858.42

3.1. Impact of PVIGR on rooftop airflow patterns

The numerical simulation utilizes a fixed southward inlet velocity of 1 m/s to characterize the aerodynamic performance of the integrated system. The choice of a low wind speed is intended to reflect the distinctive physical characteristics of urban rooftop environments. In practice, rooftop PV systems are typically installed at low elevations to minimize the structural risks associated with the high wind loads that occur at greater heights above the building envelope.

Figure 3 compares the airflow fields of the RPV and PVIGR systems. In the RPV system, the incoming flow impinges on the windward row, producing flow separation and a low-velocity wake that shields the downstream rows. At the same time, the gap between the modules and the roof surface forms a channel [16] in which the airflow accelerates. In the PVIGR system, the addition of the soil and vegetation layers reduces the sub-module clearance and increases aerodynamic resistance beneath the array. As a result, airflow obstruction becomes more pronounced, and the low-velocity region expands both beneath and behind the modules. Although the porous canopy allows some internal flow, the velocity within the vegetation layer remains much lower than the inlet wind speed. This low-momentum zone weakens the airflow reaching the downstream rows and suppresses wake development across the array. Overall, vegetation integration substantially modifies the near-array airflow structure and reduces ventilation within the PVIGR system.

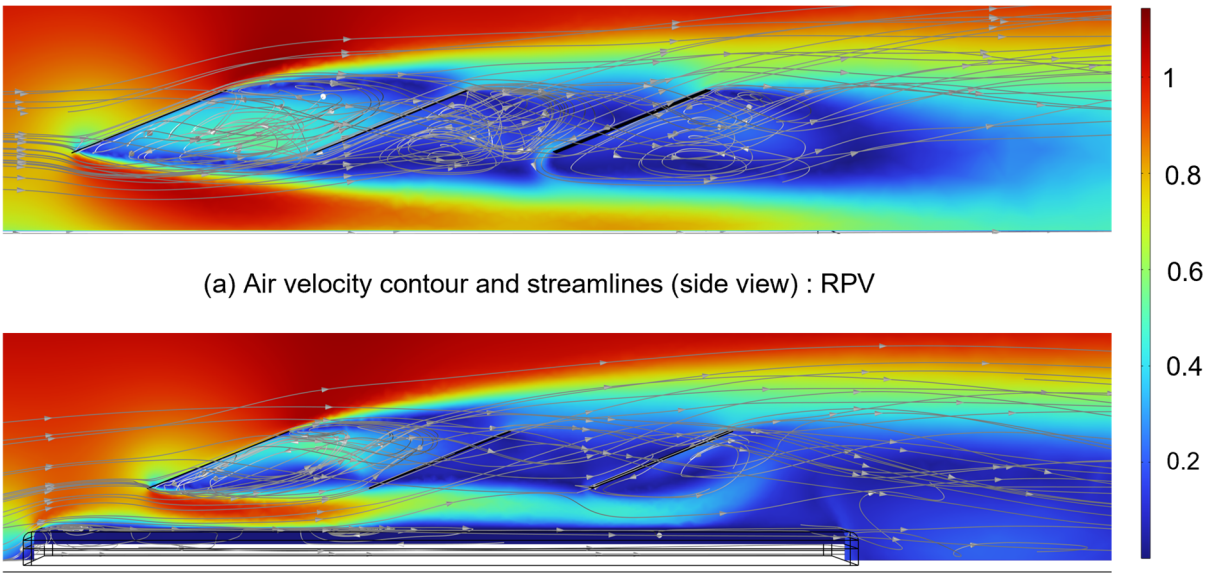

(a) Air velocity contour and streamlines (side view) : RPV

(b) Air velocity contour and streamlines (side view) : PVIGR

Figure. 3. *Cross-sectional air velocity contours and streamlines at the symmetry plane for (a) the reference RPV system and (b) the PVIGR system.*

3.2. Comparative analysis of surface temperature distributions

Figure 4 compares the transient surface temperature distributions of the PV arrays, ground and vegetation in the RPV and PVIGR systems. The results show that module temperature is strongly controlled by local ventilation conditions. In the windward first row, where the modules are directly exposed to the incoming southerly flow, the two systems exhibit similar temperature distributions. In contrast, a clear thermal divergence develops in the downstream rows. In the PVIGR system, the vegetation layer increases aerodynamic resistance within the sub-module space, resulting in lower local wind speeds and weaker convective cooling than in the RPV case. Consequently, distinct high-temperature regions form in the central and rear sections of

the array. After two hours of heating, the peak operating temperature in the PVIGR system is approximately 5 K higher than that in the RPV system, reaching about 340 K. The windward modules remain better ventilated and heat more moderately, with temperatures rising from about 323 K at 30 min to 329 K at 2 h.

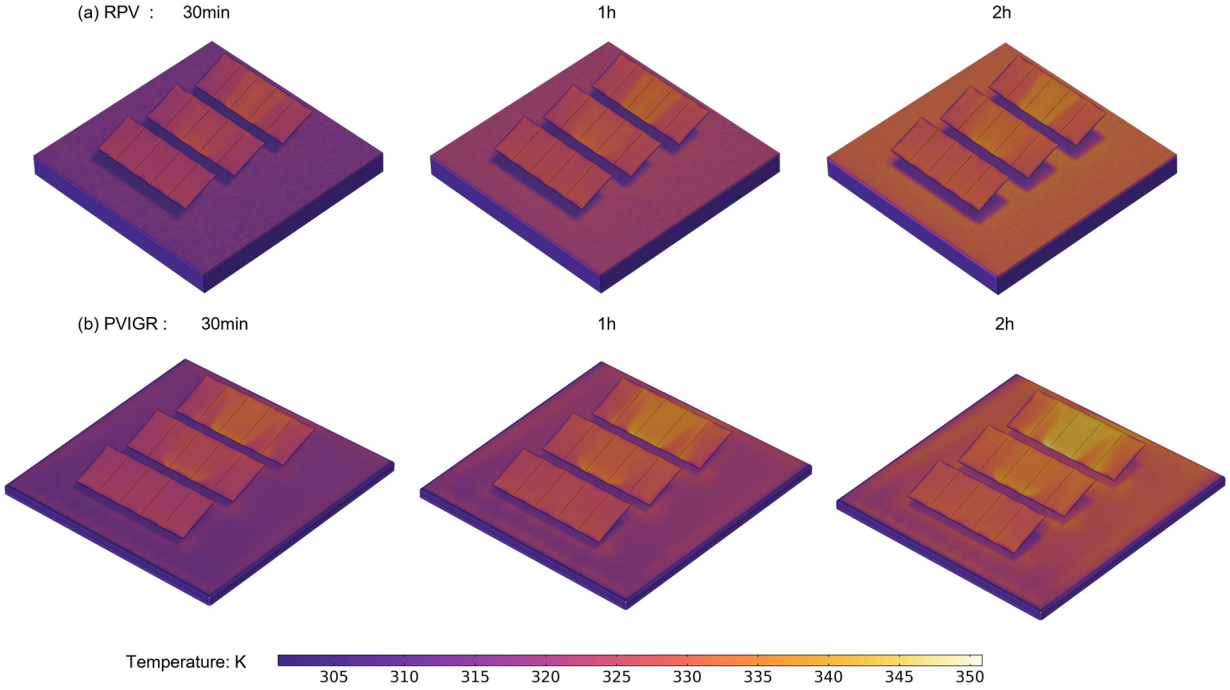

Figure. 4. *Simulated transient surface temperature distributions on the PV module upper surfaces and the vegetation canopy at 30 min, 1 h, and 2 h intervals for (a) the reference RPV system and (b) the PVIGR system.*

A comparison between the ground surface in the RPV system and the vegetation surface in the PVIGR system highlights the cooling effect of the green layer. At the beginning of the simulation, both surfaces remain at relatively low temperatures. As solar heating proceeds, the vegetation shows a greater ability to limit temperature rise through transpiration-driven latent heat dissipation. After two hours, the average temperature of the concrete surface in the RPV system reaches about 326 K, approximately 3 K higher than the vegetation surface in the PVIGR system. This cooling effect is even more pronounced in the well-ventilated windward region near the first row, where the vegetation surface is about 7 K cooler than the exposed ground. These spatial differences indicate that lower wind speeds in the rear sections of the PVIGR array constrain plant cooling performance. The elevated aerodynamic resistance around the canopy weakens heat exchange with the surrounding air, thereby limiting the full cooling potential of the vegetation.

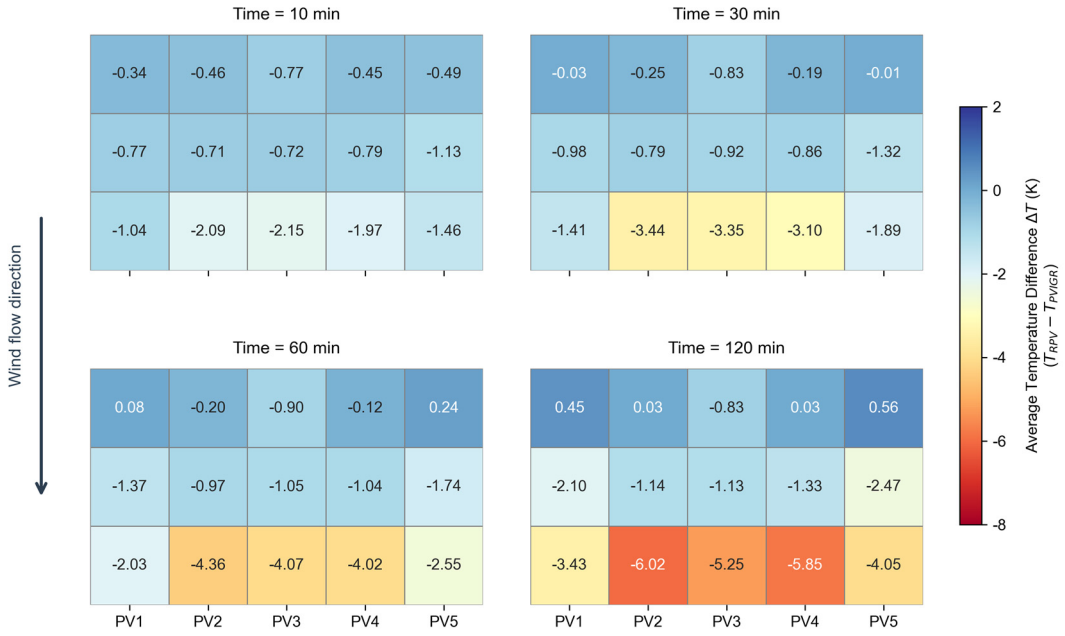

Figure. 5. *The average temperature differences ($\Delta T = T_{RPV} - T_{PVIGR}$) on the PV module back surfaces at 10, 30, 60, and 120 min intervals.*

The temperature difference at the PV backsheet provides a direct indication of how the vegetation layer affects module operation and potential electrical performance, as illustrated in Fig. 5. In the simulated configuration, the RPV system maintains lower backsheet temperatures for most modules, with the largest difference occurring at the leeward third row, where ventilation is weakest. By contrast, a measurable cooling effect from the green roof appears only in the windward first row after 30 minutes of heating. These thermal patterns indicate that sub-module ventilation is the dominant factor governing backsheet heat dissipation. The dense vegetation acts as a momentum sink, restricting airflow beneath the modules and weakening convective cooling. As a result, the maximum cooling benefit is limited to only 0.56 K for PV5 in the first row at 120 min. This suggests that the energy-generation advantage of PVIGR systems depends strongly on improving ventilation beneath the array so that vegetation-driven cooling can be more effectively translated into PV performance gains.

3.3. Analysis of relative humidity distributions

Relative humidity within the PVIGR system exhibits a pronounced spatial heterogeneity, reflecting the coupled effects of vegetation transpiration, airflow, and temperature variation, as shown in Fig. 6. Within the canopy, suppressed air movement limits the removal of transpired moisture, causing relative humidity to remain close to saturation throughout the simulation. In contrast, the region immediately above the vegetation is more effectively ventilated, which promotes vapor dispersion and maintains humidity levels closer to ambient conditions. The humidity field is also influenced by the temperature distribution within the array. As the rear rows experience greater heat accumulation during the transient process, the associated temperature rise leads to a local decrease in relative humidity. Consequently, zones of elevated temperature correspond to regions of comparatively lower relative humidity. Under the forced convection conditions considered here, the influence of vegetation-released water vapor on the broader rooftop microenvironment remains limited. The moisture-regulating effect is mainly confined to the canopy interior and the near-leaf boundary layer, indicating that transpiration contributes primarily to latent heat removal within the vegetation rather than to direct cooling of the overlying PV modules through humidity modification.

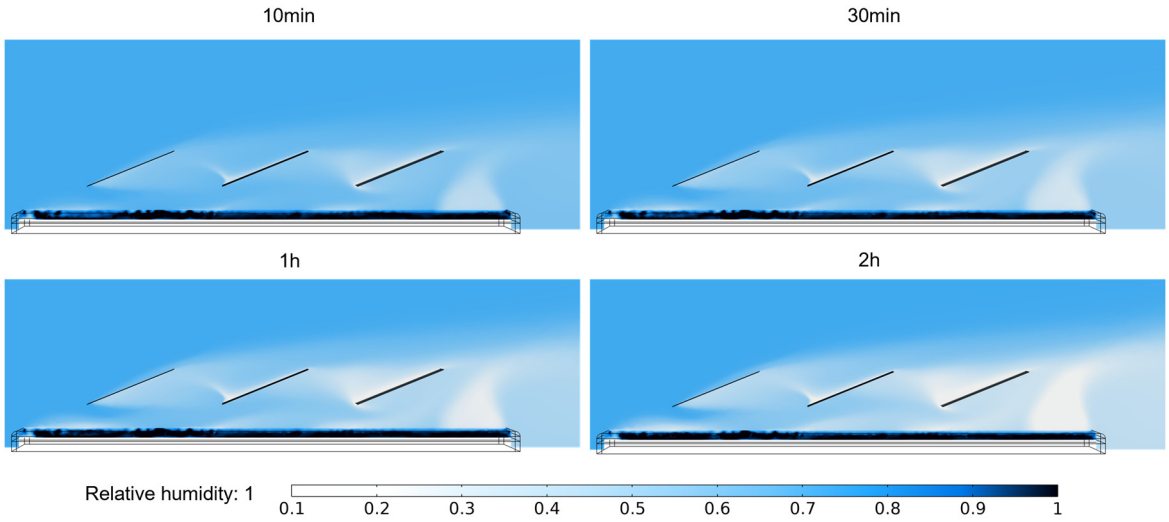

Figure. 6. *Simulated relative humidity of the PVIGR system at 10 min, 30 min, 1 h, and 2 h intervals.*

3.4. Evaluation of vegetation growing conditions

The PV array substantially alters the radiation distribution of the underlying vegetation by intercepting a large fraction of incoming solar radiation. As solar position changes, the shadow footprint shifts across the roof surface, producing strong spatial heterogeneity in canopy irradiance, as shown in Fig. 7. In unshaded regions, incident solar radiation increases from approximately 560 to 663 W/m² during the simulation, whereas shaded areas receive only about 80 W/m², mainly in the form of diffuse radiation. Consequently, vegetation within the array shadow receives only about 12% of the radiation available in unshaded areas. This pronounced reduction in radiative input alleviates thermal stress but also limits the energy available for physiological activity. The effect is strongly position dependent: vegetation near the module edges experiences intermittent shading, whereas plants beneath the central part of the array remain under prolonged low-irradiance conditions. These results indicate that radiation redistribution by the PV array is a key factor governing the microenvironment and potential growth conditions of rooftop vegetation. A more complete assessment of the long-term implications for vegetation would require simulations over extended diurnal and seasonal timescales.

The transpiration-induced latent heat sink within the canopy primarily controlled by local radiation and temperature conditions, as illustrated in Fig. 8. In the unshaded regions of the roof, the latent heat sink intensifies markedly from approximately 800 W/m³ at 10:10 to 1340 W/m³ at 12:00. In contrast, vegetation beneath the PV array exhibits weaker evaporative cooling, with values changing only from about 180 to 400 W/m³ over the same period. This difference indicates that array shading effectively reduces the thermal load on the canopy and suppresses transpiration demand. As a result, vegetation beneath the modules experiences lower water loss and a less stressful microenvironment. This effect is particularly important for extensive green roofs with shallow substrates, where plant performance is highly sensitive to evaporative water consumption.

In summary, although shading by the PV array substantially reduces incident solar radiation, it also lowers plant temperature and significantly mitigates water loss. This trade-off creates a more stable and favorable moisture regime beneath the panels, providing a distinct ecological benefit for the sustained growth of rooftop vegetation. Furthermore, these simulation results offer an important theoretical basis for future plant selection, highlighting the suitability of shade-tolerant species for maximizing the synergistic benefits of integrated rooftop systems.

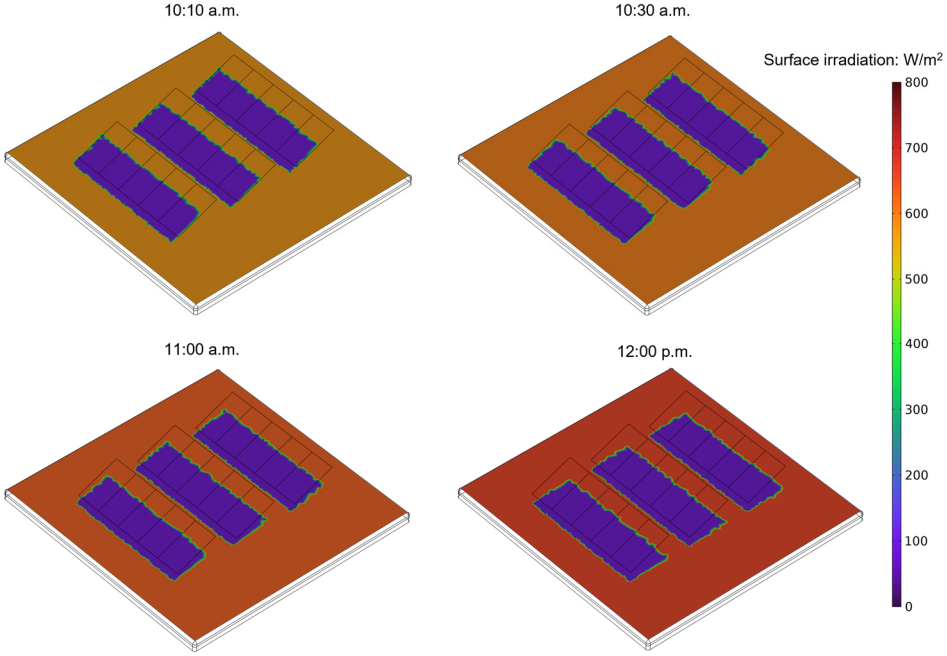

Figure. 7. *Simulated spatiotemporal distributions of solar irradiance on the vegetation surface at 10:10, 10:30, 11:00, and 12:00.*

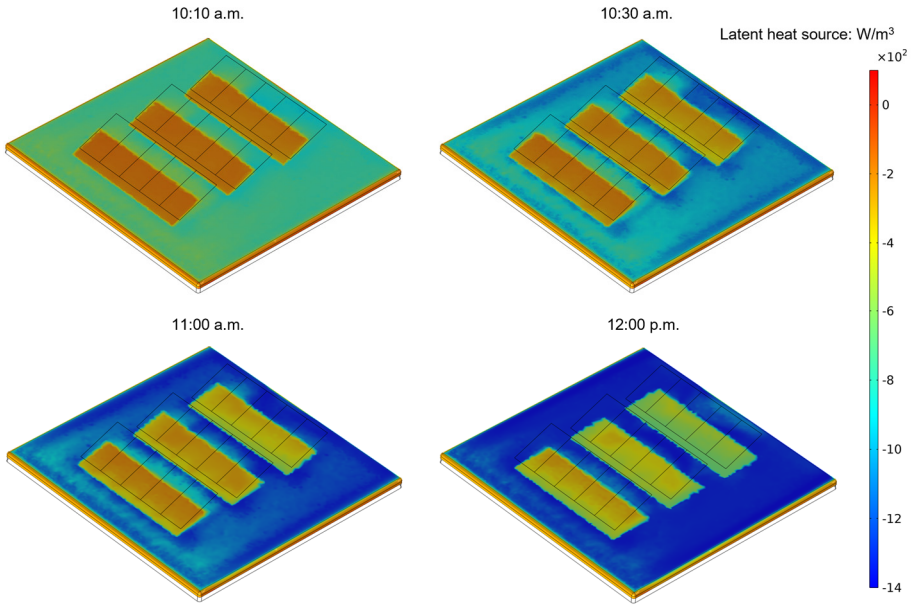

Figure. 8. *Simulated spatiotemporal distributions of vegetation latent heat absorption at 10:10, 10:30, 11:00, and 12:00.*

4. Conclusions

This study developed a three-dimensional transient multi-physics CFD model to characterize the microenvironment of a photovoltaic-integrated green roof system with a three-row PV array. The model resolves the coupled effects of airflow in free and porous media, heat and moisture transport, plant transpiration, and radiative exchange, thereby providing a numerical framework for examining the interaction between PV modules and the vegetated roof layer under realistic rooftop conditions.

Simulation results demonstrate that the vegetation significantly alters the aerodynamic characteristics and thermal conditions beneath PV modules. The porous canopy introduces flow resistance that suppresses sub-module ventilation, especially in downstream rows. In the configuration examined in this study, the resulting reduction in convective heat dissipation leads to higher PV operating temperatures. Conversely, the vegetation layer effectively cools the roof relative to a concrete surface through latent heat dissipation, while maintaining a humid intra-canopy microenvironment. Additionally, PV shading strongly reduces the incident solar radiation on the vegetation, decreasing transpiration demand and water loss while potentially altering plant physiological activity. Overall, the proposed framework successfully resolves the key physical interactions within the PVIGR system. The results indicate that the system's overall efficiency is governed by the intricate interplay of ventilation, thermal regulation, moisture conditions, and radiation redistribution. Crucially, the thermal benefit to PV performance is highly sensitive to ventilation beneath the array, which is strongly constrained by vegetation-induced aerodynamic resistance.

Future work will extend the simulations beyond the current short transient period to diurnal and seasonal timescales using measured environmental data from real operating conditions. This will enable a more comprehensive assessment of the integrated system in terms of PV power generation, vegetation growth, thermal mitigation, and water use. On this basis, subsequent research will investigate the optimization of structural and ecological design parameters, including array layout, clearance, tilt angle, and plant selection, to enhance photovoltaic conversion efficiency while maintaining environmental compatibility and the ecological functions of the green roof.

Acknowledgments

The authors gratefully acknowledge the substantial support from the Research Grants Council of the Hong Kong Special Administrative Region, China (Project No. C6003-22Y).

Nomenclature

a_1 Specific model parameter, W/m^2

a_2 Specific model parameter, W/m^2

a_3 Specific model parameter, 1/kPa^2

C_P Specific heat capacity, J/(kg·K)

c_v Vapor concentration, mol/m^3

c_{leaf} Saturated water vapor concentration within the stomatal cavity, mol/m^3

D Vapor pressure deficit, Pa

d Characteristic leaf length, m

D_0 Vapor pressure deficit constant, Pa

E_c Transpiration rate per unit leaf area, kg/(m^2·s)

F Body force term, N/m^3

f_v Blending function, dimensionless

G Volumetric moisture source term, kg/(m^3·s)

g_{lc} Liquid water capillary flux, kg/(m^2·s)

g_{w} Diffusive moisture flux, kg/(m^2·s)

G_{amb} Ambient environmental radiation, W/m^2

G_{ext} External irradiation, W/m^2

G_m Mutual radiation exchange, W/m^2

I Identity tensor, dimensionless
I_{diff} Diffuse atmospheric radiation, W/m^2
J Radiosity, W/m^2
k Turbulent kinetic energy, m^2/s^2
LAD Leaf area density, m^2/ m^3
M_v Molar mass of water vapor, kg/mol
P Turbulent kinetic energy production, W/m^3
p Pressure, Pa
q Conductive heat flux vector, W/m^2
Q_{H} Diffusive flux of thermal enthalpy, W/m^3
Q_{S} Thermal sink driven by the phase change of water during soil moisture evaporation, W/m^3
Q_{m} Mass source term, kg/(m^3·s)
$Q_{r,s-w}$ Incident shortwave solar radiation flux, W/m^2
Q_{V} Latent heat removed via transpiration, W/m^3
Q_{PV} Total volumetric heat source in the PV module arising from solar radiation absorption, W/m^3
q_s Incident direct solar radiation, W/m^2
q_r Radiative heat flux, W/m^2
r_{a} Leaf boundary layer resistance, s/m
r_{s} Stomatal resistance, s/m
$r_{\mathrm{s,min}}$ Minimum resistance value when the leaf stomata is fully open, s/m
t Time, s
T Temperature, K
u Velocity, m/s
w Total moisture content, kg/m^3

Greek symbols

β^* Turbulence model coefficient, dimensionless
γ Turbulence production coefficient, dimensionless
ε_{p} Porosity, dimensionless
ε_s Surface emittance, dimensionless
κ Permeability, m^2
μ Dynamic viscosity, Pa·s
μ_{T} Turbulent viscosity, Pa·s
ρ Density, kg/m^3
σ Stefan-Boltzmann constant, W/(m^2·K^4)
σ_k Turbulent kinetic energy Prandtl number, dimensionless
σ_ω Dissipation rate diffusion coefficient, dimensionless
ϕ Relative humidity, dimensionless
ω Specific dissipation rate, 1/s
ω_{v} Vapor mass fraction, dimensionless
τ Stress tensor, Pa

Subscripts and superscripts

a a air
amb ambient
d diffuse
eff effective
ext external
g gas phase
i index of discrete radiation direction
l liquid phase

m mutual

s surface

v water vapor

References

[1] Mohamed A, Lorestani N, Shabani F. Impact of urbanization on land surface temperature: A global perspective[J]. Current research in environmental sustainability, 2025, 10: 100315.

[2] Chen L, Zhang S, Cheng I, et al. The resilience paradox of rooftop PV: Building cooling penalties and heat risks[J]. Building and Environment, 2025, 282: 113233.

[3] Sailor D J, Anand J, King R R. Photovoltaics in the built environment: A critical review[J]. Energy and Buildings, 2021, 253: 111479.

[4] Chen L, Chang H, Zhang S, et al. Comparing designs for photovoltaic-green roofs: A year-long field study in a subtropical climate[J]. Renewable Energy, 2026: 125805.

[5] Arenandan V, Wong J K, Ahmed A N, et al. Efficiency enhancement in energy production of photovoltaic modules through green roof installation under tropical climates[J]. Ain Shams Engineering Journal, 2022, 13(5): 101741.

[6] Hui S C M, Chan S C. Integration of green roof and solar photovoltaic systems[C]//Joint symposium. 2011: 1-12.

[7] Lamnatou C, Chemisana D. A critical analysis of factors affecting photovoltaic-green roof performance[J]. Renewable and Sustainable Energy Reviews, 2015, 43: 264-280.

[8] Kaewpraek C, Ali L, Rahman M A, et al. The effect of plants on the energy output of green roof photovoltaic systems in tropical climates[J]. Sustainability, 2021, 13(8): 4505.

[9] Kohler M, Feige R, Wiartalla W. Interaction between PV-systems and extensive green roofs[J]. 2007.

[10] Hui S C M, Chan H M. Development of modular green roofs for high-density urban cities[C]//World Green Roof Congress. 2008.

[11] Cavadini G B, Cook L M. Green and cool roof choices integrated into rooftop solar energy modelling[J]. Applied Energy, 2021, 296: 117082.

[12] Žižak T, Medved S, Arkar C. Effect of solar photovoltaics on green roof energy balance and evapotranspiration[J]. Sustainable Cities and Society, 2025, 121: 106206.

[13] Shashua-Bar L, Pearlmutter D, Erell E. The cooling efficiency of urban landscape strategies in a hot dry climate[J]. Landscape and urban planning, 2009, 92(3-4): 179-186.

[14] Hang J, An L, Zhao Y, et al. Comparative simulation of transpiration and cooling impacts by porous canopies of shrubs and trees[J]. Sustainable Cities and Society, 2024, 111: 105573.

[15] Feng C, Meng Q, Zhang Y. Theoretical and experimental analysis of the energy balance of extensive green roofs[J]. Energy and buildings, 2010, 42(6): 959-965.

[16] Chang H, Dong P, Wei X, et al. Effects of photovoltaic module on wind dynamics over water surface for aquavoltaic applications[J]. Renewable Energy, 2026: 125508.